Engineering the semiconductor/oxide interaction for stacking twin suppression in single crystalline epitaxial silicon(111)/insulator/Si(111) heterostructures

New Journal of Physics
The open-access journal for physics

Engineering the semiconductor/oxide interaction for stacking twin suppression in single crystalline epitaxial silicon(111)/insulator/Si(111) heterostructures

T Schroeder[1,4], P Zaumseil[1], O Seifarth[1], A Giussani[1], H-J Müssig[1], P Storck[2], D Geiger[3], H Lichte[3] and J Dabrowski[1]

[1] IHP, Im Technologiepark 25, 15236 Frankfurt (Oder), Germany
[2] SILTRONIC AG, Hanns-Seidel-Platz 4, 81737 München, Germany
[3] Technical University of Dresden, Zellescher Weg 16, 01062 Dresden, Germany
E-mail: schroeder@ihp-microelectronics.com

New Journal of Physics **10** (2008) 113004 (21pp)
Received 10 July 2008
Published 7 November 2008
Online at http://www.njp.org/
doi:10.1088/1367-2630/10/11/113004

Abstract. The integration of alternative semiconductor layers on the Si material platform via oxide heterostructures is of interest to increase the performance and/or functionality of future Si-based integrated circuits. The single crystalline quality of epitaxial (epi) semiconductor–insulator–Si heterostructures is however limited by too high defect densities, mainly due to a lack of knowledge about the fundamental physics of the heteroepitaxy mechanisms at work. To shed light on the physics of stacking twin formation as one of the major defect mechanisms in (111)-oriented fcc-related heterostructures on Si(111), we report a detailed experimental and theoretical study on the structure and defect properties of epi-Si(111)/Y_2O_3/Pr_2O_3/Si(111) heterostructures. Synchrotron radiation-grazing incidence x-ray diffraction (SR-GIXRD) proves that the engineered Y_2O_3/Pr_2O_3 buffer dielectric heterostructure on Si(111) allows control of the stacking sequence of the overgrowing single crystalline epi-Si(111) layers. The epitaxy relationship of the epi-Si(111)/insulator/Si(111) heterostructure is characterized by a type A/B/A stacking configuration. Theoretical *ab initio* calculations show that this stacking sequence control of the heterostructure is mainly achieved by electrostatic

[4] Author to whom any correspondence should be addressed.

interaction effects across the ionic oxide/covalent Si interface (IF). Transmission electron microscopy (TEM) studies detect only a small population of misaligned type B epi-Si(111) stacking twins whose location is limited to the oxide/epi-Si IF region. Engineering the oxide/semiconductor IF physics by using tailored oxide systems opens thus a promising approach to grow heterostructures with well-controlled properties.

Contents

1. Introduction

With further aggressive scaling of microelectronic devices, silicon (Si) is running more and more into fundamental physical limits. To increase the performance and/or functionality of future Si-based integrated circuits (ICs), global and local integration approaches of alternative semiconductors (IV–IV (e.g. SiGe, SiC), III–V (e.g. GaAs, AlN) and II–VI (e.g. ZnO, CdTe)) on the Si material platform are in consequence intensively studied [1]. Global integration approaches address the deposition of functional semiconductor layers over the whole wafer structure and are typically pursued by wafer supplier companies to further develop their substrate product portfolio [2]. In contrast, integrated device manufacturers (IDMs) focus on the local integration of high-quality semiconductor layers within the processed area of the future device structure [3]–[5]. An important innovation in the field with high commercial impact are layer transfer techniques which are nowadays well suited to tackle global (e.g. silicon-on-insulator (SOI) and germanium-on-insulator (GOI) substrates via combined layer transfer and wafer bonding techniques [6, 7]) as well as local (e.g. flip-chip techniques [8], die-to-wafer-bonding [9] and microstructure printing [10]) integration tasks. The classical heteroepitaxy approach to deposit alternative semiconductor layers (e.g. GaAs [11, 12], GaN [13, 14], InP [15] etc) with high crystalline quality on Si substrates remains highly attractive due to its cost-effectiveness. For example, a recent breakthrough in setting up a cost-effective GaN materials platform was reported by the heteroepitaxial deposition of crack-free, single crystalline GaN layers on Si(001) via AlN buffer layers [16].

Dielectric oxide heterostructures on Si are another promising class of buffer materials with a wide range of properties for the integration of functional semiconductors [17]. It must however be pointed out that, to the best of our knowledge, the quality of the up to nowadays prepared semiconductor (S)–insulator (I)–Silicon (Si) heterostructures grown by two simple, subsequent oxide and semiconductor epitaxy steps has not yet achieved the level of technological relevance.

This is mainly due to the fact that the fundamental physical mechanisms of the interaction between alternative functional semiconductors of interest (i.e. SiGe and III–V materials) and the most widely used buffer dielectric materials (i.e. transition and rare earth oxides) are only poorly understood at present. Typical unsolved solid state physics issues, limiting the structural and in consequence electrical properties of such S–I–Si systems, concern for example the control of the growth mode to achieve closed, atomically smooth semiconductor layer structures, the mechanisms at work in the creation of defects in the epitaxial (epi) semiconductor film, the possibility of preparing strained semiconductor layers by heteroepitaxial overgrowth of lattice mismatched oxide buffers etc.

Recently, we introduced single crystalline, (111)-oriented Pr_2O_3–Y_2O_3 double oxide film structures on Si(111) as a flexible buffer layer system to achieve the lattice matched or mismatched integration of functional semiconductors [18]. The advantages of this mixed oxide buffer approach is given by its flexibility to engineer the lattice and interface (IF) properties, as discussed in the following. First, the (111)-oriented Pr_2O_3–Y_2O_3 double oxide films can be grown in the form of truly single crystalline epi layers, characterized especially by a twin-free type B epitaxy relationship with respect to the Si(111) substrate [18, 19]. It is noted that the type A/B heteroepitaxy nomenclature refers to the stacking sequence of fcc-related (111)-oriented heterostructures on Si(111) substrates, namely whether the (111) layers of the epi film structure exhibit the same stacking vector as the Si(111) substrate (type A) or whether a stacking fault at the epilayer/Si(111) IF rotates the stacking vector in the film by 180° around the Si(111) surface normal (type B) [20]–[22]. A unique stacking configuration of the oxide buffer is an important precondition to achieve the epi overgrowth of these buffer oxides by truly single crystalline, i.e. stacking twin-free (111)-oriented, fcc-related semiconductor layers (e.g. Si, Ge, GaAs etc). Stacking twin formation in (111)-oriented, fcc-related semiconductor epilayers, integrated on the Si(111) material platform via buffer layer systems, is one of the major defect mechanisms, severely suppressing the achievable crystalline and electrical quality of the functional semiconductor layer (e.g. epi-Si(111)/CaF_2/Si(111) [23], epi-Si(111)/hex-Pr_2O_3/Si(111) [24, 25], epi-Si(111)/CeO_2/Si(111) [26, 27] etc). The second advantage of our mixed Pr_2O_3–Y_2O_3 buffer layer approach is given by the fact that both oxides crystallize in the cubic (cub)-bixbyite oxide structure (space group: Ia-3) so that the formation of solid solutions over the whole $Pr_{2-x}Y_xO_3$ ($x = 0$ to 2) stoichiometry range is feasible [28, 29]. In consequence, with Y_2O_3 ($a = 1.0604$ nm) and Pr_2O_3 ($a = 1.1152$ nm) lattice dimensions being 2.4% smaller and 2.4% bigger, respectively, than twice the Si lattice ($2a = 1.0862$ nm), it is possible for example to study the integration of lattice matched ($Pr_{2-x}Y_xO_3$ ($x = 1$) buffer) as well as mismatched ($Pr_{2-x}Y_xO_3$ ($x \neq 1$) buffer) epi Si(111) films. The third advantage of the Pr_2O_3–Y_2O_3 double oxide buffer structure is given by the fact that Y_2O_3 is thermodynamically more stable in contact with Si than Pr_2O_3 and Y_2O_3 addition allows therefore to tailor the IF reactivity to achieve the epi Si overgrowth [30]–[32].

In this paper, we report a detailed experimental and theoretical study on the structure and defects of compressively strained epi Si(111) layers grown on lattice mismatched Y_2O_3/Pr_2O_3/Si(111) support systems. The aim of the paper is (i) to prepare stacking-twin free high-quality epi Si(111)/insulators/Si(111) heterostructures, (ii) to shed light on the fundamental physics mechanisms at work in defining the transition of the stacking information from the ionic oxide buffer to the growing covalent semiconductor layer, and (iii) to evaluate the possibility of creating strained epi Si layers via lattice mismatched oxide heterostructures.

2. Experimental

Boron-doped Si(111) substrates were cleaned by Piranha and NH_4F wet etching techniques according to a recipe recently described in detail [33]. The H-terminated Si(111) wafers were loaded into the ultrahigh vacuum (UHV) (base pressure 10^{-10} mbar) molecular beam epitaxy (MBE) facility which consists of two separated oxide and SiGe chambers. Prior to oxide deposition in the oxide MBE chamber, the sample was annealed for 5 min at 700 °C to prepare the high quality (7 × 7)-Si(111) surface [34]. The preparation of the 10 nm Pr_2O_3/10 nm Y_2O_3 thick double oxide heterostructure followed a procedure recently summarized in detail elsewhere [18, 19, 35]. In the following discussion, both metal (Me) oxides are referred to as Me_2O_3 (Me = Pr, Y) when common insulator characteristics are discussed. After preparing the Y_2O_3/Pr_2O_3/Si(111) heterostructure in the oxide MBE chamber, the sample was transferred *in situ* to the separated MBE SiGe setup to avoid the presence of metal contaminations in the epi-Si layers. Epi-Si films with thicknesses of 20 and 130 nm were grown at 625 °C on the Y_2O_3/Pr_2O_3/Si(111) support, using typically a flux of 1.5 nm min^{-1}.

An EK 35 reflection high energy electron diffraction (RHEED) apparatus from Staib instruments ($E = 15.8$ keV) as well as a VSI low energy electron diffraction (LEED) system ($E = 85$ eV) were employed to control the quality of the epi-Si layer by monitoring the Si(111)-(7 × 7) surface reconstruction. A FEI Tecnai F20 Cs-corrected transmission electron microscope (TEM) was used at TU Dresden to measure high resolution direct lattice cross-section images along the bulk Si $\langle\bar{1}10\rangle$-direction. These invasive and local TEM measurements were supplemented by *ex situ* non-destructive x-ray reflectivity and diffraction (XRR and XRD, respectively) studies which yield highly averaged, global information about the sample structure [36]. A laboratory-based Rigaku SmartLab diffractometer (Cu K_α-radiation ($\lambda = 0.154$ nm)), was used for XRR measurements to characterize the layer structure morphology of the epi-Si/insulator/Si (111) heterostructure. Typically, the x-ray footprint averages over a sample surface of about 1 cm^2. Quantitative XRR fits were performed to evaluate thickness as well as roughness root mean square (rms) values (given in nanometer (nm)) [37]. Synchrotron radiation (SR)-based XRD studies, having far superior sensitivity and resolution characteristics with respect to laboratory-based XRD equipment, were carried out at the insertion device beamline ID 32 of the European Synchrotron Radiation Facility (ESRF) to study the structure and defect characteristics of the nano-scaled epi-Si/insulator/Si (111) heterostructure [38]. Here, a *Kappa*-six circle diffractometer was used in the grazing incidence (GI) mode at an x-ray beam energy of 10.6 keV (0.117 nm). Total reflection of the incident 10.6 keV x-ray beam from Si, Y_2O_3 and Pr_2O_3 surfaces occurs below the critical angles α_c of 0.17°, 0.23° and 0.27°, respectively, allowing thus to carry out non-destructive depth profiling structure studies of the epi-Si/Y_2O_3/Pr_2O_3/Si(111) heterosystem by decreasing the incident angle α from 0.6° (bulk sensitive mode) up to 0.1° (surface sensitive mode). The XRD intensities shown hereafter are given in counts per second (cps) and are indexed in reciprocal hexagonal Si(111) surface (labelled *Surf*) HKL coordinates but the Si, Pr_2O_3 and Y_2O_3 Bragg peaks are also labelled with respect to their reciprocal cubic bulk (denoted *Bulk*) lattices [25].

Ab initio calculations were done with the *ab initio* pseudopotential plane wave code fhi96md [39]. We applied the local density approximation (LDA) for the exchange and correlation energies [40, 41] and nonlocal pseudopotentials in the Troulier–Martins scheme [42, 43] with 40 Ryd cut-off for plane waves.

3. Results

3.1. X-Ray structure studies

3.1.1. Heterostructure morphology. XRR, RHEED and LEED were applied to study the layer morphology and surface characteristics of the epi-Si/Y_2O_3/Pr_2O_3/Si(111) heterostructure.

According to the above given growth conditons, a typical XRR scan of about 20 nm thick epi-Si layer on a Me_2O_3/Si(111) heterostructure is shown in figure 1(a). For the sake of clarity, the fit (red line) is displaced on purpose from the experimental data (blue line) to demonstrate the excellent correspondence. The sketch on the right side of figure 1 shows the applied fit model which consists of an epi-Si/Y_2O_3/Pr_2O_3/IF/Si(111) multilayer system. It is noted that the IF layer between Si(111) and Pr_2O_3 consists of amorphous Pr-silicate and is formed during the hex $\rightarrow$ cub-Pr_2O_3 PT [19, 44]. Assuming bulk electron densities in the model, the quantitative analysis proves that the various layer thicknesses (bold numbers) reproduce well the targeted growth parameters of the deposited layers and that the IF roughness rms values (italic numbers) are small. Interestingly, the highest IF roughness value is found in the data fitting for the Y_2O_3/Pr_2O_3 IF. This experimental finding is probably an indirect result of the mixing of the two isomorphic oxides Y_2O_3 and Pr_2O_3 in consequence of an IF reaction at the oxide/oxide boundary, as recently detected by a detailed synchrotron radiation-grazing incidence x-ray diffraction (SR-GIXRD) [18]. Most importantly, the epi-Si layer surface roughness is very low even for an only 23 nm thick Si layer. The two-dimensional (2D) character of the epi-Si surface is demonstrated by the very streaky nature of the RHEED pattern in figure 1(b) which shows only a very small intensity modulation along the rods. The RHEED image figure 1(b) is recorded with the electron beam aligned along the Si^{Bulk} $\langle 1\bar{1}0\rangle$ azimuth and the white arrows depict the reciprocal (1×1) unit cell. Using the Si(111) substrate wafer as reference, the spacing of the observed reciprocal (1×1) unit cell points to a (111)-oriented epi-Si surface orientation. This assignment is corroborated by the observation of a (7×7) Si(111) surface reconstruction in the RHEED (white dotted lines) as well as in the LEED study (figure 1(c)). Certainly, a well-developed (7×7) surface reconstruction is an indication of the high epi-Si(111) film quality. It is noted for completeness that these results were achieved after optimization of the Si growth mode on the Y_2O_3/Pr_2O_3/Si(111) support system. Under the present growth conditions, the Si growth mode is initially characterized by Volmer–Weber behaviour but the Si multilayer growth front typically reduces towards a single layer growth mode at an epi Si layer thickness above 15 nm (data not shown). Choosing too low ($<400^\circ$) or too high ($>800^\circ$) deposition temperatures, epi-Si layers of poor quality result either due to the too low mobility of the Si deposit or the occurrence of an IF reaction towards amorphous Y-silicate, respectively.

3.1.2. Epi relationship. Wide angle XRD studies are reported in the following on a 130 nm thick epi-Si(111) layer on Y_2O_3/Pr_2O_3/IF/Si(111) support systems to determine the epi relationships of the heterostructure.

The vertical growth orientation of the epi-Si/Y_2O_3/Pr_2O_3/Si(111) heterostructure was detected by specular θ–2θ XRD scans (figure 2). The observed Si Bragg peaks are labelled at the bottom of figure 2 and all belong to the family of $(nnn;\ n = 1, 2, 3)$ Si diffraction signals. As no other Si Bragg peaks are observed, this result indirectly demonstrates that the epi-Si layer grows (111)-oriented and that its diffraction signals are therefore superimposed on the Si(111) substrate reflections. The Me_2O_3 oxide Bragg peaks are indicated on the top of

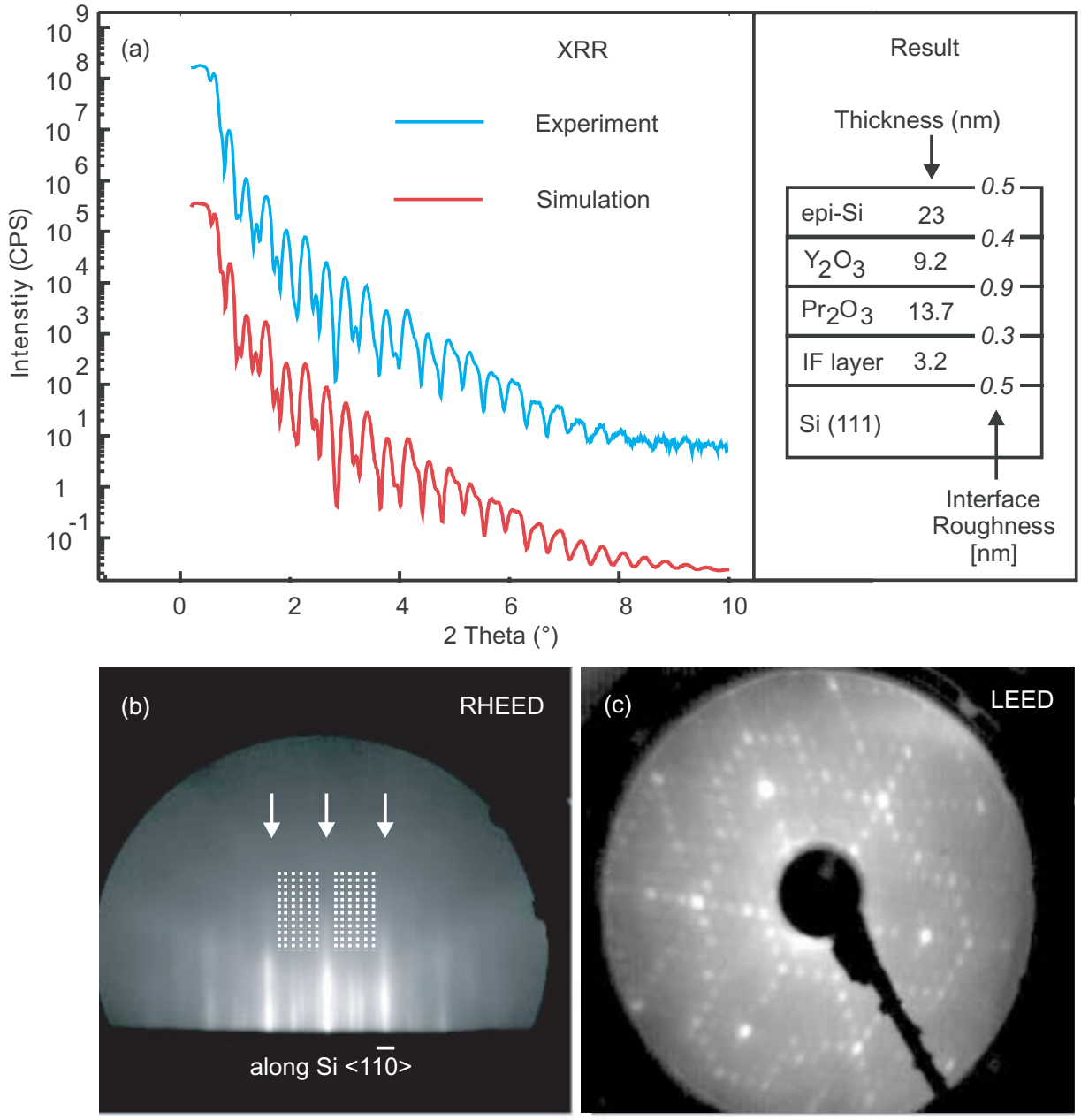

Figure 1. XRR layer morphology study on the epi-Si(111)/Me_2O_3/Si(111) heterostructure (a); RHEED (b) and LEED (c) studies on the epi-Si(111)–(7 × 7) surface reconstruction.

figure 2 and can be unambiguously assigned to the family of (*nnn*; $n = 2, 4, 6$) Bragg peaks of cub-Y_2O_3 and cub-Pr_2O_3. This result clearly demonstrates the (111)-oriented growth of the Y_2O_3/Pr_2O_3 heterostructure on Si(111) [18]. The sketch on the right side of figure 2 summarizes the vertical growth orientation of the complete epi-Si/Me_2O_3/Si(111) heterostructure. Two more insights can be gained from the analysis of the specular θ–2θ XRD scan. Firstly, the almost coincidence of the Si (*nnn*; $n = 1, 2, 3$) diffraction signals with the respective Me_2O_3

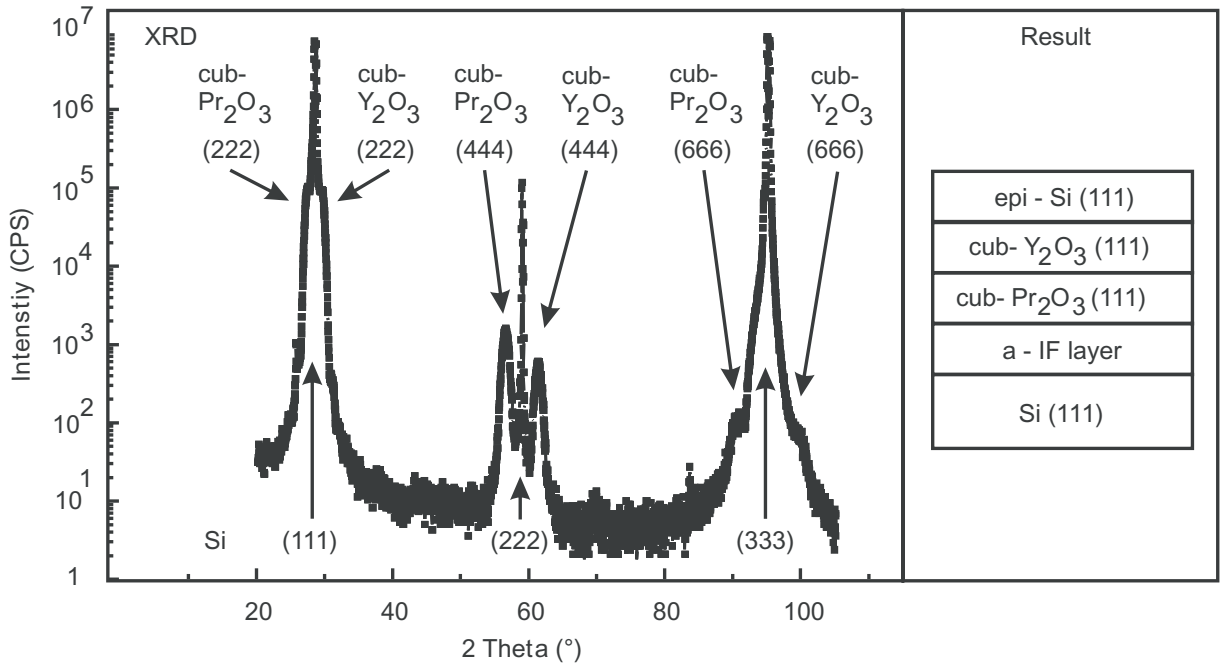

Figure 2. Specular θ–2θ XRD study to determine the vertical growth orientation of the epi-Si(111)/Y_2O_3/Pr_2O_3/Si(111) system.

(nnn; $n = 2, 4, 6$) Bragg peaks is due to the fact that the cubic bulk unit cells of Y_2O_3 and Pr_2O_3 are only about 2.4% smaller and bigger, respectively, than twice the Si lattice dimensions. For example, the Pr_2O_3 and Y_2O_3 (444) Bragg peaks are observed close to the forbidden Si(222) Bragg peak. Secondly, a precise analysis of the Me_2O_3 Bragg peak position reveals in addition that the Y_2O_3/Pr_2O_3 heterostructure is not in a fully relaxed state in the epi-Si(111)/Me_2O_3/Si(111) sandwich stack. For example, the Pr_2O_3 (444) (theory: $2\Theta^{(444)}_{Pr_2O_3} = 57.18^\circ$; $d^{(111)}_{Pr_2O_3}$: 0.6439 nm) and Y_2O_3 (444) (theory: $2\Theta^{(444)}_{Y_2O_3} = 60.44^\circ$; $d^{(111)}_{Y_2O_3}$: 0.6122 nm) Bragg peaks are observed at $2\theta = 56.47^\circ$ ($d^{(111)}_{Pr_2O_3} = 0.6512$ nm) and $2\theta = 61.31^\circ$ ($d^{(111)}_{Y_2O_3} = 0.6041$ nm), respectively. In consequence, an extension of the Pr_2O_3 (111) and a compression of the Y_2O_3 (111) lattice plane spacings is observed with respect to the bulk values. As pointed out below, this experimental finding is best explained by the compressive and tensile in-plane strains, acting in the epi-Si(111)/Me_2O_3/Si(111) sandwich stack on the Pr_2O_3 and Y_2O_3 layers, respectively [18].

The azimuthal orientation of the epi-Si/Y_2O_3/Pr_2O_3/Si(111) heterostructure was studied in figure 3 by SR-GIXRD in-plane scans ($L = 0.05$) along the high symmetry directions of the Si(111) surface, namely along the Si^{Surf} [$H00$] (Si^{Bulk} $\langle 11\bar{2}\rangle$) (left panel) and the Si^{Surf} [$HK0$] (Si^{Bulk} $\langle 01\bar{1}\rangle$) (right panel) azimuth. Both directions were studied in the bulk ($\alpha = 0.6^\circ$) and surface ($\alpha = 0.1^\circ$) sensitive GIXRD mode. The Si^{Surf} [$H00$] scan at $\alpha = 0.6^\circ$ in the left panel reports at $H = 1$ and 2 the Si crystal truncation rod (CTR) signals and at $H = 3$ the true Si ($22\bar{4}$) Bragg peak. The Me_2O_3 diffraction signals at $\alpha = 0.6^\circ$ are observed at about $H = 0.75$, 1.5, 2.25 and 3 which can be assigned to the ($\bar{1}\bar{1}2$), ($\bar{2}\bar{2}4$), ($\bar{3}\bar{3}6$) and ($\bar{4}\bar{4}8$) Bragg peaks, respectively. It is seen that these Me_2O_3 Bragg peaks are completely suppressed in the surface sensitive Si^{Surf} [$H00$] scan at $\alpha = 0.1^\circ$, allowing thus to study the (111)-oriented epi-Si layer without any

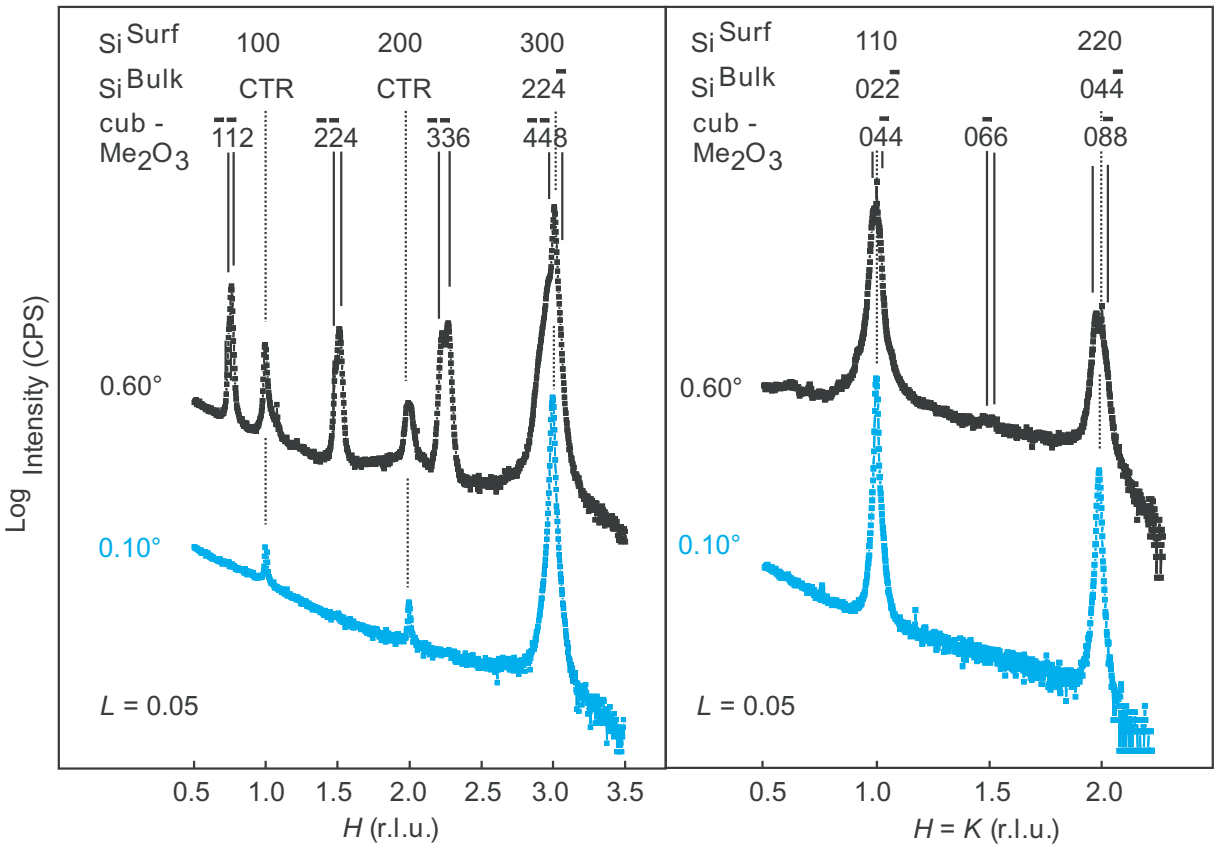

Figure 3. GI-XRD study along the Si^{Surf} [100] ($Si^{Bulk}[11\bar{2}]$) (left) and Si^{Surf} [110] ($Si^{Bulk}[01\bar{1}]$) (right) in-plane direction to determine the azimuthal orientation of the epi-Si(111)/Y_2O_3/Pr_2O_3/Si(111) heterostructure.

influence from the Si(111) substrate. The epi Si(111) layer shows along the Si^{Surf} $[H00]$ scan the same diffraction signal as in case of the bulk sensitive measurement, namely besides the CTR signals at $H = 1$ and 2 only the Si $(22\bar{4})$ Bragg peak at $H = 3$ is observed. In consequence, it can be concluded that the $\langle 11\bar{2}\rangle$ azimuth of the epi-Si(111) layer (as well as of the Si(111) substrate) coincides with the $\langle \bar{1}\bar{1}2\rangle$ in-plane direction of the Me_2O_3 buffer layers. To further corroborate these results on the azimuthal orientation of the epi-Si/Y_2O_3/Pr_2O_3/Si(111) heterostructure study, the complementary Si^{Surf} $[HK0]$ azimuthal direction was studied in addition (right panel). Here, the Si^{Surf} diffraction signals are observed in the bulk sensitive measurement ($\alpha = 0.6^\circ$) at $H = K = 1$ and 2, corresponding both to true Si bulk Bragg peaks, namely the $(02\bar{2})$ and $(04\bar{4})$ diffraction, respectively. The cub-Me_2O_3 Bragg peaks $(0\bar{4}4)$ and $(0\bar{8}8)$ closely coincide at about $H = K = 1$ and 2 with these bulk Si Bragg peaks, resulting in a broadening of the observed diffraction signals. The forbidden Me_2O_3 Bragg peaks $(0\bar{6}6)$ are indicated for completeness at about $H = K = 1.5$ but give rise to only negligible diffraction intensity above the background. The surface sensitive measurement at $\alpha = 0.1^\circ$ along the Si^{Surf} $[HK0]$ azimuth results in a complete suppression of the strong Me_2O_3 Bragg peaks $(0\bar{4}4)$ and $(0\bar{8}8)$ so that only the narrow Bragg peaks of the epi-Si layer are observed. Clearly, the only visible epi-Si layer Bragg peaks are observed at $H = K = 1$ and 2 so that these diffraction signals can be unambiguously assigned to the Si $(02\bar{2})$ and $(04\bar{4})$ Bragg peaks. In consequence, it can be concluded that the

$\langle 01\bar{1}\rangle$ azimuth of the epi-Si(111) layer (as well as of the Si(111) substrate) coincides with the $\langle 0\bar{1}1\rangle$ in-plane direction of the Me_2O_3 buffer layers. It is noted that the here given antiparallel alignment of the Si and Me_2O_3 azimuths is due to their exclusive type B epitaxy relationship, as outlined further below.

3.1.3. High resolution strain study.. Non-destructive depth profiling SR-GIXRD studies by varying the incident angle α of the x-ray beam on the sample surface were applied to detect with high resolution the in-plane strain in the buried Y_2O_3/Pr_2O_3 heterostructure as well as in the epi-Si(111) film.

For this purpose, by varying the incident angles α from the bulk sensitive ($\alpha = 0.6^\circ$) to the surface sensitive ($\alpha = 0.1^\circ$) mode, the Me_2O_3 $(\bar{3}\bar{3}6)$ in-plane Bragg peaks were studied along the Si^{Surf} $[H00]$ (Si^{Bulk} $\langle 11\bar{2}\rangle$) azimuth (figure 4(a)) and the Me_2O_3 $(0\bar{8}8)$ as well as the Si $(04\bar{4})$ in-plane Bragg peaks were scanned along the complementary Si^{Surf} $[HK0]$ (Si^{Bulk} $\langle 01\bar{1}\rangle$) azimuth (figure 4(b)). The positions of the cub-Pr_2O_3 $(\bar{3}\bar{3}6)$, cub-Y_2O_3 $(\bar{3}\bar{3}6)$ and Si $(04\bar{4})$ Bragg peaks are indicated by dashed–dotted, dashed–double dotted and solid lines, respectively. The most important result in figures 4(a) and (b) is the fact that the experimentally detected $(\bar{3}\bar{3}6)$ and $(0\bar{8}8)$ Bragg peak positions of the buried Y_2O_3/Pr_2O_3 heterostructure underneath the epi-Si(111) film substantially deviate from the theoretically expected bulk values. Theoretically, the cub-Pr_2O_3 $(\bar{3}\bar{3}6)$ and $(0\bar{8}8)$ Bragg peaks in figures 4(a) and (b), respectively, are expected at $H = 2.192$ ($d^{\bar{3}\bar{3}6}_{Pr_2O_3} = 0.1518\,\text{nm}$) and $H = K = 1.948$ ($d^{088}_{Pr_2O_3} = 0.0986\,\text{nm}$). However, the experimentally found cub-Pr_2O_3 in-plane Bragg peak positions are situated for all α values at rather constant higher reciprocal space values, namely for the cub-Pr_2O_3 $(\bar{3}\bar{3}6)$ Bragg peaks in figure 4(a) at $H = 2.218$ ($d^{\bar{3}\bar{3}6}_{Pr_2O_3} = 0.1499\,\text{nm}$) and in case of the cub-Pr_2O_3 $(0\bar{8}8)$ diffraction signals in figure 4(b) at $H = K = 1.976$ ($d^{088}_{Pr_2O_3} = 0.0972\,\text{nm}$). This compression of the Pr_2O_3 in-plane parameter is probably a consequence of the interaction of the Pr_2O_3 film with the smaller Si and Y_2O_3 lattices. Accordingly, the interaction between the Y_2O_3 film and the bigger Pr_2O_3 and Si lattices results on the other hand in an extension of the Y_2O_3 in-plane spacings. Theoretically, the bulk cub-Y_2O_3 $(\bar{3}\bar{3}6)$ and $(0\bar{8}8)$ Bragg peaks in figures 4(a) and (b), respectively, are expected at $H = 2.305$ ($d^{\bar{3}\bar{3}6}_{Y_2O_3} = 0.1443\,\text{nm}$) and $H = K = 2.049$ ($d^{088}_{Y_2O_3} = 0.09373\,\text{nm}$). The peaks are shifted for all α values towards lower reciprocal space parameters, namely the cub-Y_2O_3 $(\bar{3}\bar{3}6)$ Bragg peaks in figure 4(a) are found at $H = 2.267$ ($d^{\bar{3}\bar{3}6}_{Y_2O_3} = 0.1467\,\text{nm}$) and the cub-$Y_2O_3$ $(0\bar{8}8)$ diffraction signals are detected in figure 4(b) at $H = K = 2.026$ ($d^{088}_{Y_2O_3} = 0.0948\,\text{nm}$). It is noted that, due to the almost constant Me_2O_3 $(\bar{3}\bar{3}6)$ and $(0\bar{8}8)$ Bragg peak positions as a function of α, the detected strain in the Y_2O_3 and Pr_2O_3 layers is rather homogeneously distributed over the whole oxide film thicknesses. In this respect, the non-destructive depth profiling study on the epi-Si/Y_2O_3/Pr_2O_3/IF/Si(111) heterostructure by changing the information depth with the help of the incident angle α results only in a change of the Y_2O_3/Pr_2O_3 Bragg peak intensity ratio in figures 4(a) and (b). In particular, as the Y_2O_3 film is situated on top of the Pr_2O_3 layer, decreasing α results in an increase of the Y_2O_3/Pr_2O_3 Bragg peak intensity ratio. Interestingly, when the incident angle $\alpha = 0.1^\circ$ is below the critical angle $\alpha_c^{Si} = 0.17^\circ$ for total reflection of the x-ray beam from the closed epi-Si(111) layer structure, the complete suppression of the Me_2O_3 $(\bar{3}\bar{3}6)$ Bragg peaks is observed in figure 4(a). This result guarantees that the observed Si $(04\bar{4})$ Bragg peak at $\alpha = 0.1^\circ$ in figure 4(b) is entirely due to the epi-Si(111) layer. In consequence, the SR-GIXRD allows also to study the strain properties of the epi-Si(111) layer without any influence from the oxide

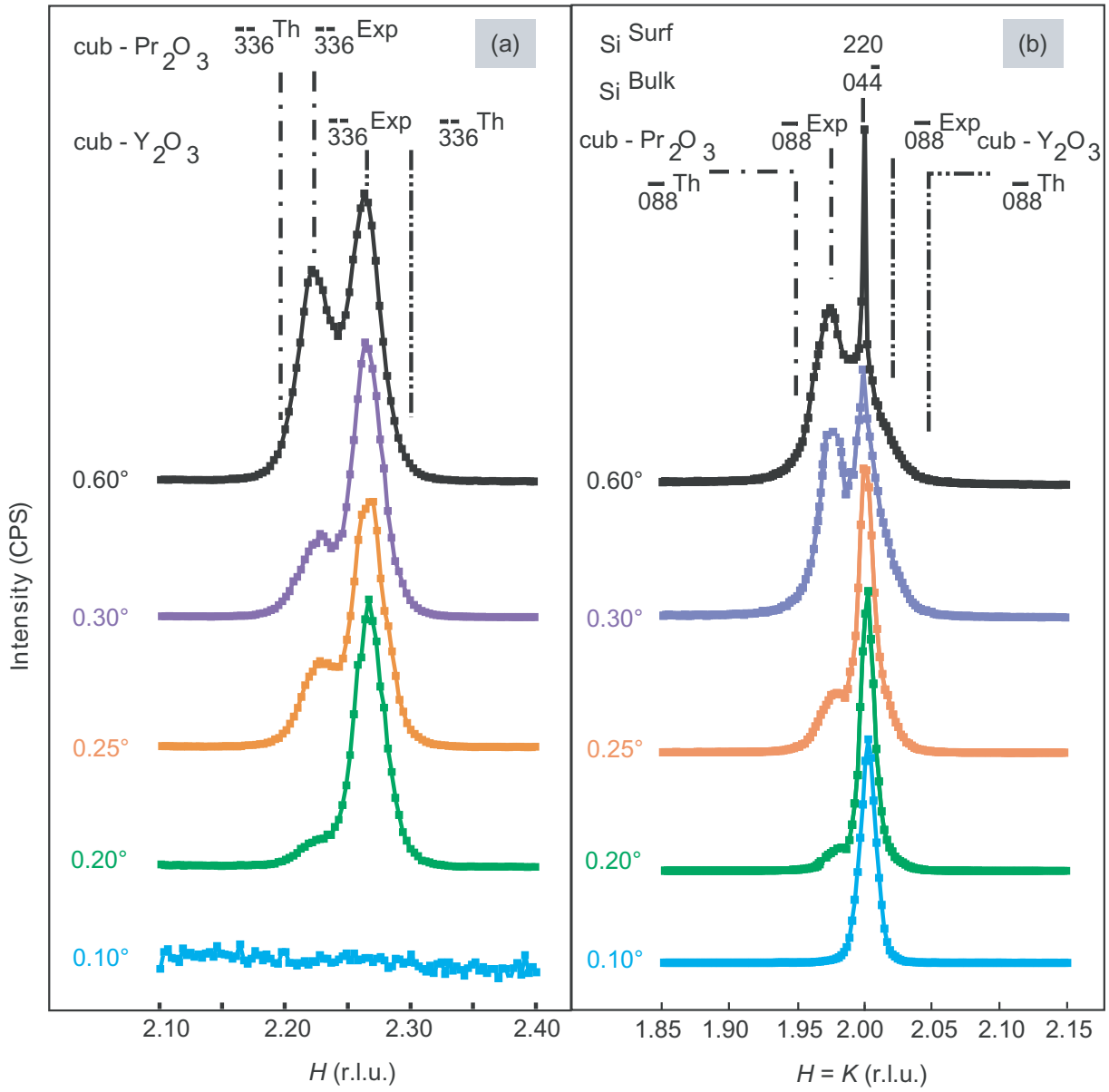

Figure 4. Non-destructive high resolution depth profiling GI-XRD study on the Me_2O_3 $(\bar{3}\bar{3}6)^{Bulk}$ (a) and the Me_2O_3 $(0\bar{8}\bar{8})^{Bulk}$ as well as $Si(04\bar{4})^{Bulk}$ (b) in-plane reflections to determine strain effects in the epi-layer system.

heterostructure and the Si(111) substrate wafer. A quantitative analysis of the experimental Si $(04\bar{4})$ Bragg peak position ($H = K = 2.002$; $d_{Si}^{044} = 0.0958$ nm) in figure 4(b) shows that the smaller Y_2O_3 film lattice underneath results only in a small in-plane compression of about 0.1% in the epi-Si(111) layer along the Si^{Surf} $[HK0]$ (Si^{Bulk} $\langle 01\bar{1}\rangle$) azimuth with respect to Si bulk values ($H = K = 2$; $d_{Si}^{044} = 0.09601$ nm). Furthermore, the full-width at half-maximum (FWHM) of the epi-Si $(04\bar{4})$ Bragg peak allows to deduce an average in-plane domain size of approximately 100 nm in the grown epi-Si layer structure. An identical quantitative analysis was carried out on the epi-Si $(22\bar{4})$ Bragg peak along the complementary Si^{Surf} $[H00]$ (Si^{Bulk} $\langle 11\bar{2}\rangle$)

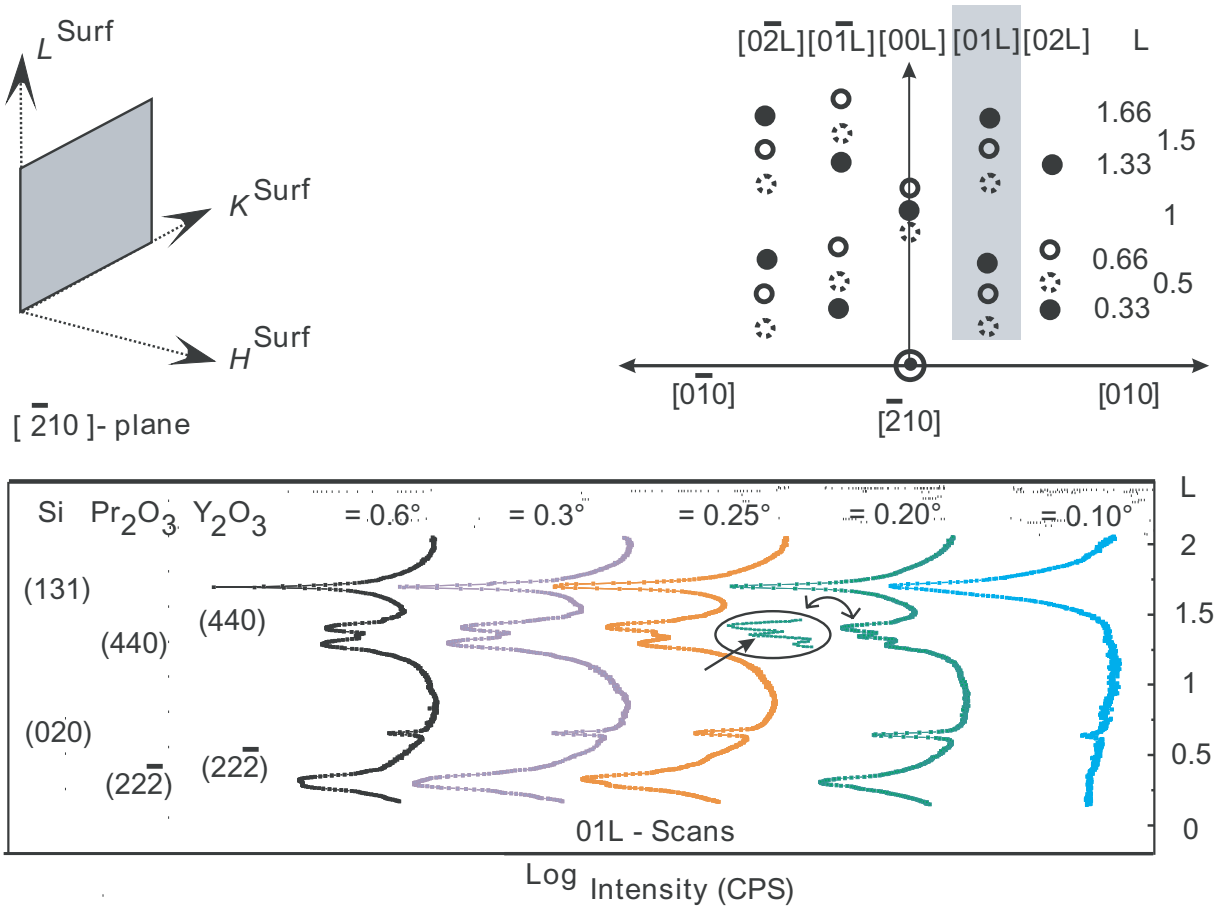

Figure 5. Non-destructive depth profiling GI-XRD study along the $[01L]^{Surf}$ rod to determine the stacking order in the epi-Si(111)/Y_2O_3/Pr_2O_3/Si(111) heterostructure.

azimuth (data not shown) and resulted in similar values for the in-plane strain as well as the average domain size of the epi-Si(111) film.

3.1.4. Stacking sequence study. A further important structure property of the epi-Si(111) layer on the $Y_2O_3/Pr_2O_3/Si(111)$ heterostructure concerns its stacking sequence along the (111) growth direction, i.e. whether it grows in a bicrystalline twinned or in a single crystalline untwinned configuration. This phenomenon can be studied by stacking sensitive out-of plane SR-GIXRD rod scan measurements, as summarized in figure 5. The sketch shows the location of the *KL* lattice plane in the reciprocal hexagonal Si^{Surf} coordinate system. Furthermore, the Bragg peak intensity distribution is given in the $Si^{Surf}KL$ lattice plane for an epi-Si $(111)/Y_2O_3/Pr_2O_3/Si(111)$ heterostructure which is characterized by an exclusive type A/B/A epitaxy relationship. Assuming bulk lattice parameters, cub-Pr_2O_3 and cub-Y_2O_3 Bragg peaks are sketched by dashed and solid open circles, respectively; Si diffraction signals are depicted by filled black circles. The grey panel in the sketch highlights the position of the stacking sensitive out-of-plane $[01L]$ rod in the $Si^{Surf}KL$ lattice plane which was studied as an example in this work in the range from $L = 0$ to 2. The indexing of the Bragg peaks, situated on this

out-of-plane $[01L]^{Surf}$ rod from $L = 0$ to 2, is given in the figure adjacent to the experimental data. To unveil the stacking sequence in the epi-Si(111) layer as a function of depth, the experimental data of $[01L]$ rod scans was collected for various incident angles α in the range from $\alpha = 0.6^\circ$ (bulk sensitive) to 0.1° (surface sensitive). The bulk sensitive measurement at $\alpha = 0.6^\circ$ is characterized by the presence of the $Si^{Bulk}(131)$ Bragg peak at $L = 1.66$; the forbidden $Si^{Bulk}(020)$ reflection ($L = 0.66$) is only very weakly visible. The oxide heterostructure exhibits at $\alpha = 0.6^\circ$ a broad unresolved diffraction signal centred at about $L = 0.33$, which can be attributed to the poorly resolved type B $(22\bar{2})$ Bragg peaks of Pr_2O_3 ($L = 0.28$) and Y_2O_3 ($L = 0.38$). Furthermore, well-resolved double oxide peak structures are observed at $\alpha = 0.6^\circ$ on the $[01L]^{Surf}$ rod which are composed of the type B (440) Bragg peaks of Pr_2O_3 ($L = 1.28$) and Y_2O_3 ($L = 1.38$). Non-destructive depth profiling studies by decreasing α towards the critical angle for total reflection of the 10.6 keV x-ray beam from Y_2O_3 ($\alpha_c^{Y_2O_3} = 0.23^\circ$) results, due to the laminar morphology of the Y_2O_3/Pr_2O_3 oxide buffer, in an increase of the type B (440) Y_2O_3 Bragg peak ($L = 1.38$) and an attenuation of the type B (440) Pr_2O_3 Bragg peak ($L = 1.28$), as can be deduced for example by a comparison of the $[01L]^{Surf}$ rod scans at $\alpha = 0.6^\circ$ and 0.2°. A close inspection of the type B (440) Me_2O_3 Bragg peak region in the $[01L]^{Surf}$ rod scans at $\alpha = 0.2^\circ$ reveals however at $L = 1.33$ the appearance of a third Bragg peak structure. This peak is indicated in figure 5 by the arrow in the zoomed region and can be unambiguously assigned to a (131) Bragg peak of type B twins in the epi-Si(111) layer. This result of the $[01L]^{Surf}$ rod scan measurement at $\alpha = 0.2^\circ$ demonstrates that stacking twins are formed in the epi-Si(111) layer. The location of these stacking twin domains in the epi-Si(111) layer is however limited to the epi-Si/oxide boundary. This result is proven in figure 5 by recording the $[01L]^{Surf}$ rod scan at $\alpha = 0.1^\circ$ below the critical angle $\alpha_c^{Si} = 0.17^\circ$ for total reflection of the x-ray beam from the closed epi-Si(111) layer structure. Here, the type B Me_2O_3 $(22\bar{2})$ and (440) Bragg peaks of the oxide buffer on the $[01L]^{Surf}$ rod scan are completely suppressed, demonstrating that the information depth (<50 nm) of the probing x-ray beam in the $\alpha = 0.1^\circ$ configuration is clearly below the epi-Si(111) layer thickness (130 nm). In consequence, the $[01L]^{Surf}$ rod scan at $\alpha = 0.1^\circ$ probes only the upper thickness range of the epi-Si(111) layer. The observed epi-Si(111) Bragg peak distribution is identical with the one found at $\alpha = 0.6^\circ$ for the Si(111) substrate, namely the diffraction signals at $L = 0.33$ and 1.33 correspond to the forbidden Si(020) and the allowed Si(131) Bragg peaks. This result and the fact that no stacking twin Bragg peaks are observed (e.g. at $L = 1.33$) prove that the upper part of the epi-Si layer is truly single crystalline and exhibits an exclusive type A stacking sequence with respect to the Si(111) substrate.

To quantify this result, off-plane Φ scans were performed at $\alpha = 0.1^\circ$ and 0.15° by turning the sample around the Si(111) surface normal over a wide angular range, whereas the x-ray beam under a grazing incident geometry and the detector are set to fulfil the reflection condition of the Si(131) Bragg peak family ($L = 1.66$). A single crystalline epi-Si(111) film with the diamond structure (space group: $Fd-3m$) is expected to show in these measurements the threefold $\langle 111 \rangle$ rotation axis symmetry, while a bicrystalline type A/B epi-Si(111) stacking twin structure would inevitably result in a sixfold $\langle 111 \rangle$ rotation axis symmetry. The result of the off-plane Φ scan study is summarized in figure 6. It is seen in figure 6 that the off-plane Φ scan at $\alpha = 0.1^\circ$ (dotted line) with a sampling depth of about 50 nm in the epi-Si(111) layer structure detects only the expected threefold off-plane symmetry of the type A Si(131) Bragg peak family at $\Phi = -120^\circ$, 0° and 120°. This result confirms the single crystalline nature of the upper part of the type A-oriented epi-Si(111) layer, as already discussed in the $[01L]^{Surf}$

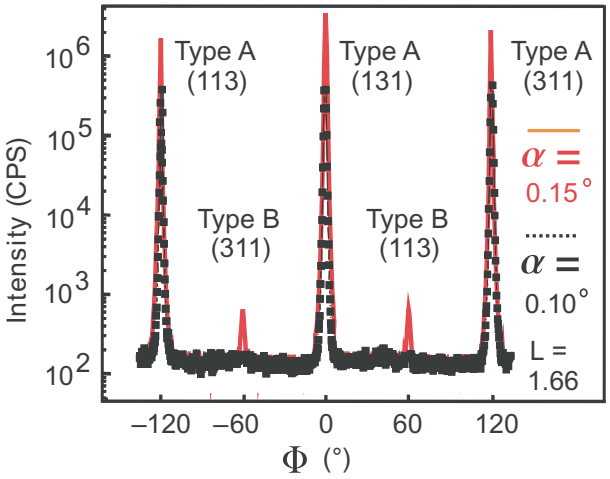

Figure 6. GI-XRD out-of-plane Φ-scan study ($L = 1.66$) on the familiy of Si $(131)^{Bulk}$ Bragg peaks at various incident angles α to determine the quantity and location of stacking twins in the epi-Si(111) layer.

rod scan study in figure 5. In contrast, a clear sixfold symmetry is detected in the off-plane Φ scan at $\alpha = 0.15^\circ$ (solid line) which is characterized by a sampling depth of about 100 nm in the 130 nm thick epi-Si(111) Bragg peak layer structure. This is true because, besides the strong type A Si(131) Bragg peaks ($> 10^6$ cps) at $\Phi = -120^\circ$, 0° and 120°, weak type B Si(131) Bragg peaks ($<10^3$ cps) are additionally detected at $\Phi = -60^\circ$ and 60°. Due to the fact that type A and type B epi-Si layer Bragg peaks in this study belong to the same Bragg peak family, a simple intensity comparison of type A and type B epi-Si layer Bragg peaks allows to give an estimate of the misaligned type B twin population in the preferentially type A-oriented epi-Si(111) layer structure. It is found that less than 0.1% of the epi-Si(111) layer structure is crystallized in the vicinity of the epi-Si/oxide IF in the misaligned type B stacking configuration.

3.2. TEM studies

Figure 7 summarizes the TEM cross section study of an epi-Si(111)/Y_2O_3/Pr_2O_3/Si(111) heterostructure with an epi-Si(111) thickness of about 40 nm, projected along the stacking sensitive $[1\bar{1}0]$ azimuth. The coordinate system of the study is depicted in the overview image in figure 7(a). Figure 7(a) shows an epi-Si(111)/Me_2O_3/Si(111) heterostructure which is characterized by the presence of closed layer structures with smooth surfaces and IFs. Figure 7(b) shows a direct lattice cross section image to visualize the type A/B/A epitaxy relationship of the epi-Si(111)/Me_2O_3/Si(111) system. The inclined dotted arrows are included in figure 7(b) to indicate the net plane normal orientation of the $(11\bar{1})$ lattice planes visible in the fcc-related Si and oxide structures in the form of lattice fringes. Obviously, the Si$(11\bar{1})$ lattice planes (black dotted arrows) in the Si(111) substrate and the epi-Si(111) structure show according to the type A epitaxy relationship an identical orientation. The type B stacking order of the Me_2O_3(111) heterostructure with respect to Si(111) results in an orientation of the Me_2O_3 $(11\bar{1})$ lattice planes (white dotted arrow) which only becomes identical to the Si$(11\bar{1})$ lattice fringes after a 180° rotation around the Si [111] surface normal. Besides the type A/B/A epitaxy relationship, the high resolution TEM image in figure 7(c) is reported to study the various IFs in the epi-Si(111)/Y_2O_3/Pr_2O_3/Si(111) heterostructure. As already reported in previous

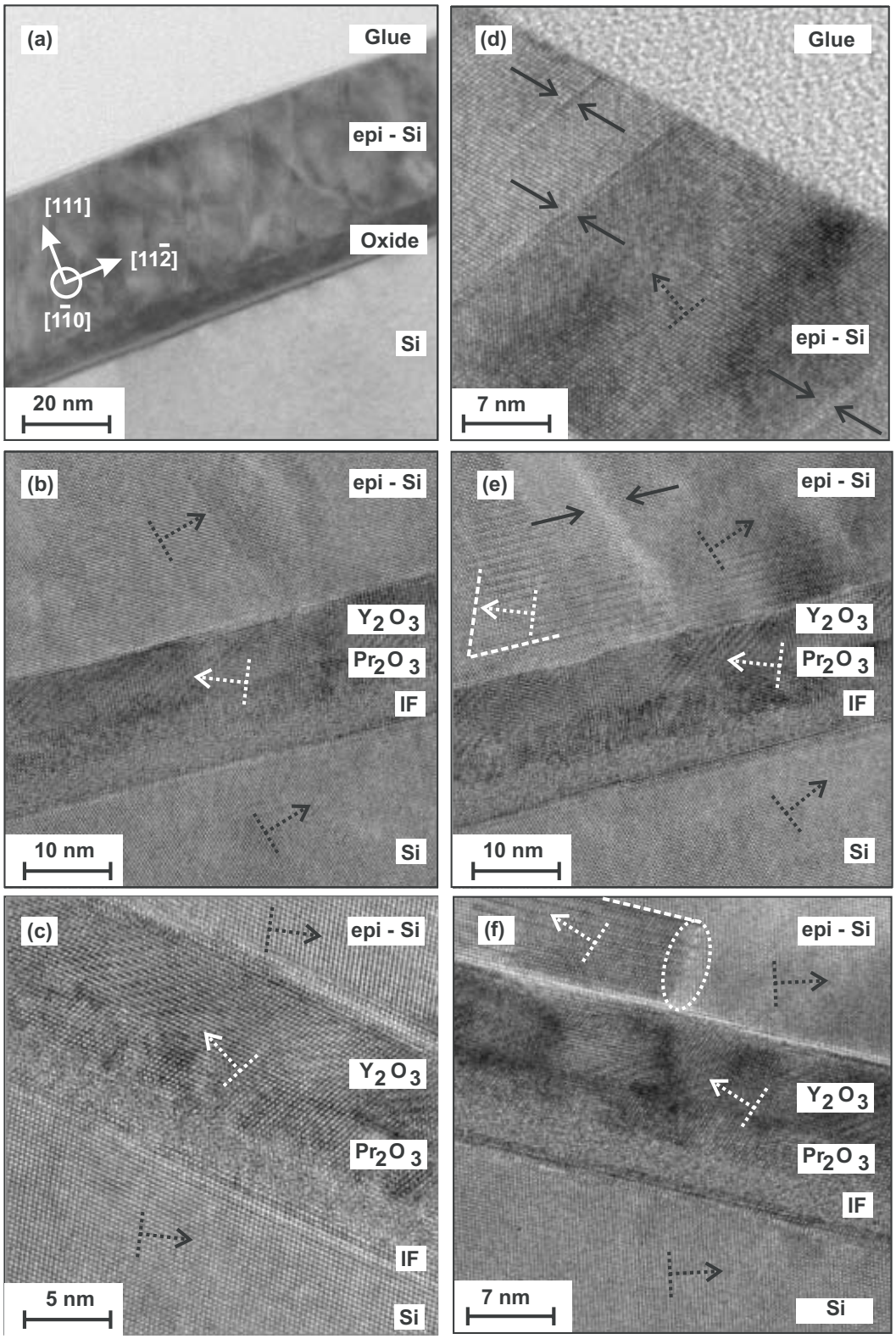

Figure 7. TEM cross-section study along the stacking sensitive Si $\langle 1\bar{1}0 \rangle$ azimuth to study the structure (a)–(c) and defect characteristics (d)–(f) of the epi-Si(111)/Y_2O_3/Pr_2O_3/Si(111) heterostructure.

studies [18, 44], the hex → cub Pr_2O_3 phase transition results in a post-deposition oxidation of the Pr_2O_3/Si(111) IF, giving rise to an amorphous Pr-silicate IF structure of about 2 nm thickness. The high resolution image (figure 7(c)) shows furthermore that the Y_2O_3/Pr_2O_3 IF region is not characterized by the presence of a sharp oxide/oxide boundary but it rather demonstrates a homogeneous transition, pointing to the presence of a compositionally graded oxide/oxide IF structure. This TEM result is in line with a recent SR-GIXRD study on the Y_2O_3/Pr_2O_3/Si(111) system which indicates the formation of a mixed $Pr_{2-x}Y_xO_3$ ($x = 0$ to 2) IF layer in the course of the isomorphic oxide-on-oxide epitaxy of Y_2O_3 on Pr_2O_3 [18]. The high epi quality of the epi-Si(111)/Y_2O_3 IF is shown in figure 7(c). Clearly, by the changing orientation of the $(11\bar{1})$ lattice planes in Y_2O_3 and the epi-Si, the image visualizes the stacking fault at the epi-Si(111)/Y_2O_3 boundary, giving rise to the type A/B epitaxy relationship. Figure 7(d) shows the surface region of the epi-Si(111) layer. Besides the atomically smooth epi-Si(111) surface, crystal defects in form of stacking faults, whose positions are indicated by black solid arrows, are clearly visible. Recently, modern XRD techniques were applied by our group to derive a highly averaged, global characterization of the stacking fault structure in the epi-Si(111) layer [47]. The TEM study shows that stacking faults are often found to thread from the epi-Si(111)/Y_2O_3 IF to the epi-Si(111) surface region and a typical example is indicated in figure 7(e). The solid black arrows indicate the height shift of two adjacent epi-Si(111) grains with respect to each other, driven by a partial dislocation of the $1/6\langle\bar{1}\bar{1}2\rangle$ type in the Si$(11\bar{1})$ slip plane. Probably, these dislocations are induced by terrace steps of atomic height on the oxide support. An alternative stacking fault creation mechanism is certainly given by plastic relaxation of the epi-Si(111) film to relax lattice and thermal misfit. Furthermore, the Volmer–Weber growth mode during the initial nucleation stage of the epi-Si layer on the oxide heterostructure can also result in lattice defects in the epi-Si(111) film. It is well known that the nucleation of misaligned film material on the facets of islands provides a low-energy path for the creation of stacking faults in epi-layer systems with respect to the classical picture of defect creation by plastic relaxation after growth beyond the critical thickness values (a model only correctly describing the film behaviour in case of an ideal layer-by-layer growth mode) [45]. A further crystal defect within the mostly type A stacked epi-Si(111) film structure (black dotted arrow) in the form of a type B Si micro-twin grain (white dotted arrow) is imaged on the left of figure 7(e) in the close vicinity of the epi-Si(111)/oxide boundary. It is seen that, after initial nucleation of the epi-Si(111) film structure in the dominant type A stacking sequence, the stacking vector is inverted and the type B Si micro-twin grain is formed. The white dashed lines in the form of an open triangle structure mark the {111} mirror plane boundaries of the type B microtwin within the type A epi-Si(111) layer. However, due to the Si crystal structure, such a low energy boundary cannot be formed along the $[11\bar{2}]$ lattice planes where type A and B twins meet (open side of the triangle structure). The stacking conflict of the type B micro-twin with respect to the surrounding type A epi-Si(111) film results thus in the formation of a defective region, giving rise in the TEM image to the formation of a moiré pattern-like transition structure in the adjacent regions [46]. Such a stacking conflict situation along $[11\bar{2}]$ lattice planes of type A and type B Si twins is also visible in figure 7(f). It shows a further type B Si micro-twin grain structure (dotted white arrow) which, in contrast to the situation in figure 7(e), grows directly on the epi-Si(111)/Y_2O_3 IF. The type B Si micro-twin structure (dotted white arrow) is nucleated in the left part and joined in the middle of the image to the type A epi-Si(111) film structure (dotted black arrow) via $[11\bar{2}]$ lattice planes, resulting in a defective stacking conflict arrangement at the centre of the dotted ellipse structure. The upper end of the type B Si twin

is indicated by a horizontal white dashed line which marks again the type B to type A stacking sequence shift, forming a (111) mirror plane boundary in the epi-Si(111) film.

In summary, the TEM study on the structure and defect characteristics of the epi-Si(111)/Y_2O_3/Pr_2O_3/Si(111) heterostructure locally corroborates the results of a recent, highly averaging XRD defect study [47].

3.3. Theory studies

Theoretical calculations were applied to gain a deeper understanding of the heteroepitaxy mechanisms at work in stabilizing the type B epitaxy relationship between the Si(111) structures and the Me_2O_3 (111) oxide films. In the following, the discussion of figure 8 will be focused on the interaction of the cub-Pr_2O_3 (111) film with Si(111) but can be applied in an analogous way to the cub-Y_2O_3(111)/Si(111) IF. Figure 8(a) shows the type B cub-Pr_2O_3(111)/Si(111) structure model where praseodymium oxide (dark blue) is connected to the Si(111) substrate through oxygen atoms (yellow): all valence orbitals of Si which are not saturated by Si atoms are used in covalent bonds with oxygen atoms of the oxide. In order to conserve the charge neutrality of the IF, all oxygen vacancy sites in the IF layer of cub-Pr_2O_3 have to be filled with oxygen; otherwise, the metal atoms in the IF layer donate electrons to silicon, the IF becomes metallic, and the IF energy increases. So exactly this amount of oxygen is needed to fill the vacancy sites and in that way keep the IF semiconducting. This implies that the IF structure does not depend on the oxidation state of the praseodymium oxide film. No matter if the film is Pr_2O_3, PrO_2, or PrO_x, the first layer of the oxide on top of silicon consists of $Pr^{+III}O_2$. That is, oxygen and metal atoms occupy the sites of the CaF_2 structure (as in cub-PrO_2), but the light blue metal atoms at the IF are all in the Pr^{+III} state (as in Pr_2O_3) and not in the Pr^{+IV} state (as in PrO_2). Geometrically, the IFs of the type A and type B cub-Pr_2O_3(111)/Si(111) structures differ by the stacking order of (111) layers, namely the essential difference between these configurations is the relative position of metal atoms in the first layer of the oxide and unoxidized Si atoms in the first and second (111) double layers. Figure 8(b) shows the registry of Pr and Si atoms in type A (left) and type B (right) IFs; top and side views are given in the upper and lower panels, respectively. Oxygen atoms are not shown for clarity. In type A IF, Pr atoms from the first oxide layer sit above Si atoms from the second (111) double-layer of Si. In type B IF, Pr atoms from the first oxide layer sit above Si atoms from the first (111) double-layer of Si. Figure 8(c) shows that the type A (left) and type B (right) geometries are associated with a different strength of the electrostatic interaction between the metal atoms and the electrons in Si–Si bonds at the IF (indicated by thick black lines) as well as with the Si core. In B-type configuration (right), the positively charged Pr ion is repelled by four Si cores to which it is equidistant, whereas in A-type configuration (left) the Pr ion is repelled by six Si cores. Three of the latter are the same distance from Pr as in the B-type configuration, and the other three are further away. By summing up the electrostatic energies one finds that the core–core electrostatic repulsion is stronger in the IF of type A. On the other hand, the A-type Pr ion is attracted electrostatically by electrons in six Si–Si bonds, while the B-type Pr ion is attracted by only three Si–Si bonds (although the centres of weight of these bonds are closer to the Pr ion in the IF B). By summing up these electrostatic contributions one estimates that the IF of type B has noticeably lower energy than the IF of type A. Assuming that the electrostatic charge of Pr is $+3e$, that the charge of the bond may be approximated by a bond-centre point charge of $-0.5e$, that the effective charge of the Si core is thus $+e$, and that screening of the

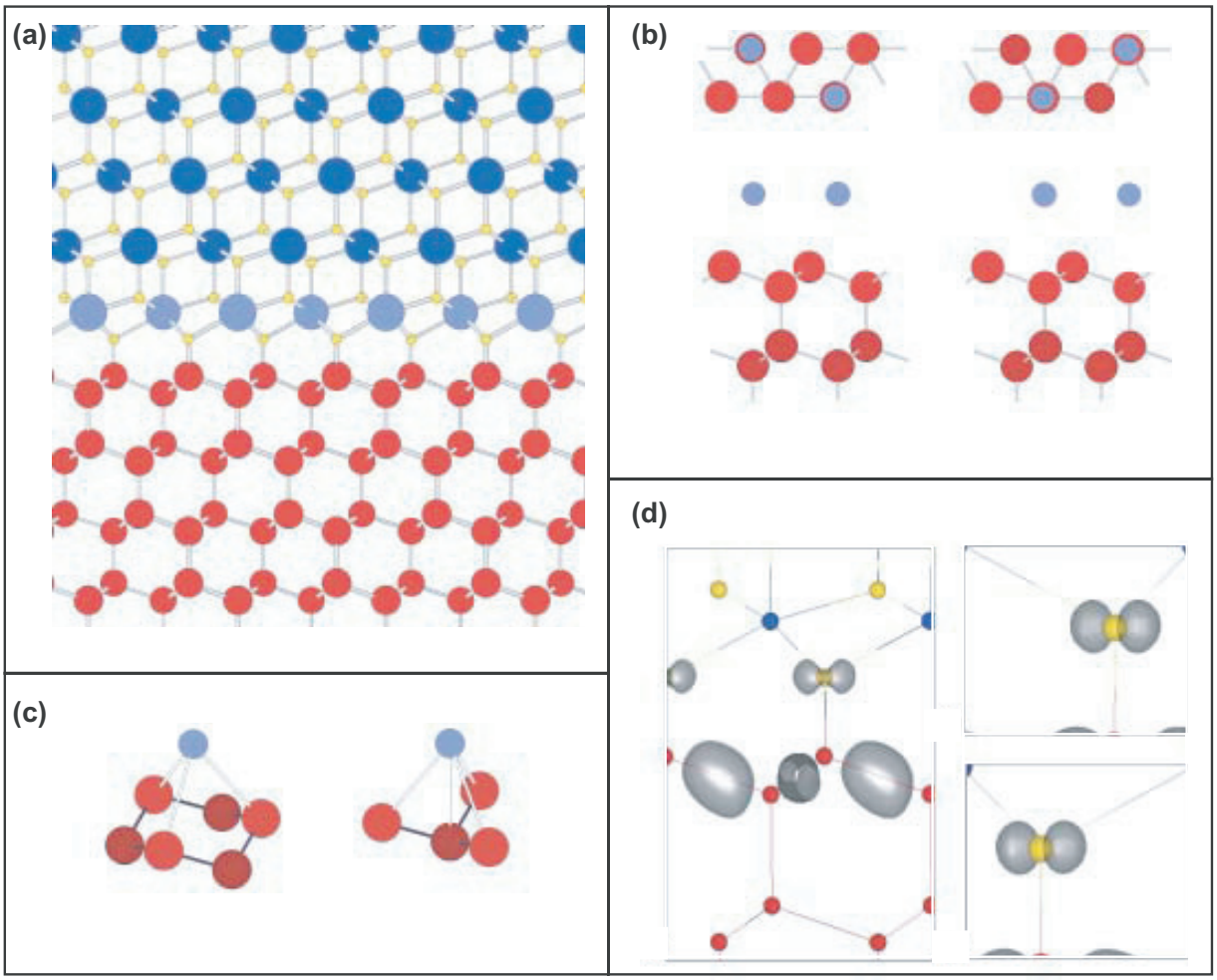

Figure 8. *Ab initio* calculations to evaluate the energy of type A and B stacking configurations at the ionic Me_2O_3/covalent Si(111) IF; structure model of the type B-oriented Pr_2O_3 (111)/covalent Si(111) boundary (a); registry of Pr and Si atoms in type A (left) and type B (right) IF; top and side views are given in upper and lower panels, respectively (b); Pr–Si interaction configuration in type A (left) and type B (right) geometry (c); role of electronic IF states at the Pr_2O_3/Si(111) boundary (d).

electrostatic interaction between Pr and the substrate takes place with the computed dielectric constant $k = 14$ of Si [48, 49], the type B cub-Pr_2O_3(111)/Si(111) IF geometry is favoured over the type A configuration by approximately 50 meV per IF Pr atom. One obtains nearly the same result when the electron charge is assumed to be evenly distributed along the Si–Si bond. In these estimates, interatomic distances as obtained from *ab initio* structural optimization of the IF have been used: the distance between Pr and Si is 6.74 Bohr (shorter) and 7.95 Bohr (longer), the Si–Si bond length is 4.40 Bohr, and the Pr–Si–Si angle in type-A configuration is assumed to be 90° (the calculation yields 88.2°). In the optimized structure, the shorter Pr–Si distances are all the same within less than 0.03 Bohr. The *ab initio* energy difference (40 meV per IF Pr) is close to this estimate. This value is well converged. In fact, it depends only weakly on numerical conditions (basis set, k-point sampling and number of Pr layers) and is basically the same for

PrO_2 and Pr_2O_3 films. The agreement between the estimated and the calculated values, and the weak dependence of the *ab initio* result on the details of the electronic structure (as evidenced by easily achievable convergence) confirm that the B-type IF is mainly stabilized by electrostatics. This agreement also indicates that there is no strong enhancement of short-range electrostatic screening at the IF. Since electrons in the backbonds form IF resonances, one may expect that, being largely decoupled from the rest of the crystal, they are more easily polarizable than bulk electrons. One of these IF states is shown in the left panel of figure 8(d). However, the interatomic distances and angles between the atoms contributing to the IF states are largely independent of the type of the IF, and so is the charge localized on oxygen orbitals. This result is shown on the right of figure 8(d), where the top and bottom panels depict the charge localized on oxygen in type A and B configurations, respectively. It is noted that the application of this theoretical treatment to the cub-Y_2O_3(111)/Si(111) IF structure allows the derivation of a similar result, namely that electrostatics results in a clear stabilization of the type B IF configuration. It is found that the quantitative values are smaller in case of the cub-Y_2O_3(111)/Si(111) IF by a factor of two, a result probably driven by the smaller ionic character of Y_2O_3 with respect to Pr_2O_3.

4. Conclusion and outlook

It was reported in the past that epi Si(111) layers can be grown on hex-Pr_2O_3(0001) films on Si(111) [24]. However, these layers suffer from the fact that the hex-Pr_2O_3(0001) buffer oxide films suppress the stacking information of the Si(111) substrate so that the epi Si(111) layers are characterized in consequence by poor long-range order due to stacking twin formation [25]. In order to transport the stacking information to the epi Si(111) layer, the buffer oxide system was engineered by inducing a hex $\rightarrow$ cub-Pr_2O_3 phase transition [50], resulting under optimized growth conditions in the preparation of twin-free, single crystalline Pr_2O_3 (111) layers with an exclusive type B stacking orientation on Si(111) [19]. In addition, the functionality of the buffer oxide heterostructure was increased by preparing single crystalline $Pr_{2-x}Y_xO_3$ ($x = 0$ to 2) solid state solutions on Si(111) out of the isomorphic cub-Y_2O_3 and cub-Pr_2O_3 phases [18]. In consequence, the Y_2O_3–Pr_2O_3 heterostructure approach allows a flexible variation of important buffer layer parameters, i.e. lattice constants can be varied to study lattice matched and mismatched semiconductors as well as the IF reactivity can be tailored to improve the wetting of the buffer oxide by the semiconductor and avoid parasitic IF reactions.

In this study, we focus on the structure of single crystalline epi Si(111) layers on lattice mismatched Y_2O_3–Pr_2O_3 bilayer heterostructures on Si(111), i.e. on the transfer of the stacking information between the engineered ionic buffer heterostructure and covalent Si(111). The resulting epi Si(111)/Y_2O_3/Pr_2O_3/Si(111) heterostructure is atomically smooth, exhibits a (7×7) surface reconstruction and single crystalline nature, characterized by a type A/B/A stacking relationship. Theoretical *ab initio* calculations identified the electrostatic interaction across the ionic oxide/covalent Si IF as the main driving force for the stabilization of this A/B/A stacking configuration in the epi-Si(111)/insulator/Si(111) heterostructure. Interestingly, as the type A and B stacking at the oxide/Si boundary can be viewed as a local cubic ABC... and hexagonal ABA... stacking structure, respectively, this result can be compared on the basis of the simple Born–Mayer equation with ionic crystals. For the same charge and atomic distance values, the Born–Mayer equation predicts a preference of the wurtzite (hexagonal ABA... over the zinc-blende (cubic ABC...) structure due to the higher Madelung constant A (wurtzite: $A = 1.641$; zinc-blende: $A = 1.638$) [51]. Indeed, it is a well-established result of theoretical

structure calculations on III–V materials that the preference of the wurtzite over the zinc-blende structure correlates with the ionic character of the compound semiconductor [52, 53].

In addition, compressive strain creation in the epi-Si layer structure by the lattice mismatched $Y_2O_3/Pr_2O_3/Si(111)$ heterostructure was studied with high resolution by non-destructive depth profiling GI-XRD studies. Theoretically, Y_2O_3 is by about 2.4% smaller than twice the Si bulk lattice parameter but the non-destructive depth profiling GI-XRD detected an extension of the Y_2O_3 lattice by about 1.7% due to the interaction with the bigger Pr_2O_3 and Si lattices. In consequence, a compressive strain of about 0.7% could be expected at maximum in the growing epi-Si layer but GI-XRD detected only a deviation of 0.1%. It is thus obvious that the creation of strain in the epi-Si layer with the help of lattice mismatched oxide heterostructures cannot be directly derived from bulk lattice parameters but compliant effects in the buffer oxide require to strictly control the interplay of the semiconductor and oxide buffer stiffnesses. An epi-Si film thickness-dependent combined Raman and GI-XRD study is currently under way to study this point in more detail.

Furthermore, two kinds of defect structures, namely stacking twins and stacking faults, were detected in the epi-Si(111) layer structure. Misaligned type B-oriented Si twin domains account for less than 0.1% of the total quantity of the deposited epi-Si(111) layer structure and the location of these stacking twin defects is restricted to the vicinity of the oxide/Si boundary. This observed location is in line with the fact that the defect energy of stacking twins is far higher than in the case of stacking faults so that, as for example nicely demonstrated by Ernst *et al* in case of GaP heteroepitaxy on Si [45], stacking twins tend to nucleate at the IF but do not grow with the thickening film structure. In contrast, stacking faults do and the threading behaviour of stacking faults from the oxide buffer through the epi-Si(111) layer up to the surface region is also observed in the present case. Indeed, a recent XRD study was applied to investigate the stacking fault structure of the epi-Si(111) layer and a clear linear correlation of the intensity of stacking fault derived XRD signals with film thickness was detected [47]. Future work will concentrate on defect engineering approaches to improve the long-range order of the epi-Si(111) layer structure on the lattice mismatched $Y_2O_3/Pr_2O_3/Si(111)$ support system. Special emphasize will be given to approaches to tailor the surface structure of the oxide buffer in order to suppress the identified stacking fault formation mechanisms in the epi-Si(111) layer, namely the nucleation of stacking faults by the oxide roughness and by the initially formed Si island structures. In this respect, surface modification epitaxy is currently employed to (i) reduce the oxide surface roughness and (ii) to improve the Si wetting behaviour.

Certainly, progress in the preparation of high quality semiconductor/insulator/Si heterostructures by engineered oxide heterostructures is expected to also push ahead the controlled study of new revolutionary device physics concepts based on the tremendous diversity of solid state phenomena encountered in complex oxide systems (electric field effects in correlated oxide systems [54], correlated electron physics in transition metal oxides [55], all-oxide electronics [56, 57] etc).

Acknowledgments

We acknowledge financial and infrastructure support from the partners DFG, SILTRONIC, Hasylab and ESRF. The *ab initio* calculations were performed on IBM Regatta p690+ in Jülich, Germany, in the framework of project hfo06 sponsored by the Neumann Institute for Computing.

References

[1] Waser R 2003 *Nanoelectronics and Information Technology—Advanced Electronic Materials and Novel Devices* (New York: Wiley)
[2] Fitzgerald E A 2006 Engineered substrates for electronic and optoelectronic systems *Silicon Heterostructure Handbook* ed J Cressler (Boca Raton, FL: CRC Press) chapter 6
[3] Cressler J (ed) 2006 *Silicon Heterostructure Handbook* (Boca Raton, FL: CRC Press)
[4] Fang A W, Park H, Kuo Y-H, Jones R, Cohen O, Liang D, Raday O, Sysak M N, Paniccia M J and Bowers J E 2007 *Mater. Today* **10** 28
[5] Steckl A J, Park J H and Zavada J M 2007 *Mater. Today* **10** 20
[6] Tong Q Y and Gösele U 1998 *Semiconductor Wafer Bonding—Science and Technology* (New York: Wiley-VCH)
[7] Celler G K and Cristoloveanu S 2003 *J. Appl. Phys.* **93** 4955
[8] Mitze T *et al* 2005 Hybrid integration of III/V lasers on a SOI optical board *2nd IEEE Int. Conf. on Group IV Photonics*
[9] Roelkens G *et al* 2007 *Mater. Today* **10** 36
[10] Benkendorfer K, Menard E and Carr J 2007 *Compound Semicond.* **13** 16
[11] Fischer R, Morkoc H, Neumann D A, Zabel H, Choi C, Otsuka N, Longerbone M and Erickson L P 1986 *J. Appl. Phys.* **60** 1640
[12] Fang S F, Adomi K, Lyer S, Morkoc H, Zabel H, Choi C and Otsuka N 1990 *J. Appl. Phys.* **68** R31
[13] Lahreche H, Vennegues P, Tottereau O, Laugt M, Lorenzini P, Leroux M, Beaumont B and Gibart P 2000 *J. Cryst. Growth* **217** 13
[14] Joblot S, Feltin E, Beraudo E, Vennegues P, Leroux M, Omnes F, Laugt M and Cordier Y 2005 *J. Cryst. Growth* **280** 44
[15] Fehly D, Schlachetzki A, Bakin A S, Guttzeit A and Wehmann H H 2001 *IEEE J. Quantum. Electron.* **37** 1246
[16] Schulze F, Dadgar A, Bläsing J, Hempel T, Diez A, Christen J and Krost A 2006 *J. Cryst. Growth* **289** 485
[17] Ogale S (ed) 2005 *Thin Films and Heterostructures for Oxide Electronics (Multifunctional Thin Film Series)* (Berlin: Springer)
[18] Schroeder T, Costina I, Storck P, Wilke A, Seifarth O, Giussani A, Müsig H J and Zaumseil P 2008 *J. Appl. Phys.* **103** 084102
[19] Schroeder T, Zaumseil P, Weidner G, Dabrowski J, Müssig H-J and Storck P 2006 *J. Appl. Phys.* **99** 014101
[20] Ohmi S I, Tsutsui K and Furukawa S 1994 *Japan. J. Appl. Phys.* **33** 1121
[21] Sokolov N S, Alvarez J C, Shusterman Yu V, Yakovlev N L, Overney R M, Itoh Y, Takahashi I and Harada J 1996 *Appl. Surf. Sci.* **104** 402
[22] Wang C R, Müller B H and Hofmann K R 2002 *Thin Solid Films* **410** 72
[23] Olmstead M A 1999 *Thin Films: Heteroepitaxial Systems* (Singapore: World Scientific) chapter 5 p 211
[24] Tarsa E J, Speck J S and Robinson McD 1993 *Appl. Phys. Lett.* **63** 539
[25] Schroeder T, Zaumseil P, Weidner G, Lupina G, Wenger Ch, Müssig H-J and Storck P 2005 *J. Appl. Phys.* **98** 123513
[26] Kim C G 2000 *J. Vac. Sci. Technol.* B **18** 2650
[27] Elmasry N A, Hunter M, Elnaggar A and Bedair S M 2004 *J. Appl. Phys.* **98** 106104
[28] McCullough J D and Britton J D 1952 *J. Am. Chem. Soc.* **74** 5225
[29] Keith M L and Roy R 1954 *Am. Mineral.* **39** 1
[30] Lupina G, Schroeder T, Dabrowski J, Wenger Ch, Mane A, Müssig H-J, Hoffmann P and Schmeisser D 2006 *J. Appl. Phys.* **99** 114109
[31] Paumier F, Gaboriaud R J and Kaul A R 2002 *Cryst. Eng.* **5** 169
[32] Gaboriaud R J, Paumier F, Pailloux F and Guerin P 2004 *Mater. Sci. Eng.* B **109** 34

[33] Schaefer A, Schroeder T, Lupina G, Borchert Y, Dabrowski J, Wenger Ch and Bäumer M 2007 *Surf. Sci.* **601** 1473
[34] De Renzi V, Biagi R and del Pennino U 2002 *Surf. Sci.* **497** 247
[35] Jeutter N M, Moritz W, Sidorenko A and Stierle A 2007 *Appl. Phys. Lett.* **90** 062906
[36] Zaumseil P and Schroeder T 2005 *J. Phys. D: Appl. Phys.* **38** A179
[37] Zaumseil P *IHP, Rocking and Reflectivity Curve Simulation Software RCRefSimW*
[38] Als-Nielsen J and McMorrow D 2001 *Elements of Modern X-Ray Physics* (New York: Wiley)
[39] Bockstedte M, Kley A, Neugebauer J and Scheffer M 1997 *Comput. Phys. Commun.* **107** 187
[40] Ceperley D M and Alder B J 1980 *Phys. Rev. Lett.* **45** 567
[41] Perdew J P and Zunger A 1981 *Phys. Rev.* B **23** 5048
[42] Haman D R 1989 *Phys. Rev.* B **40** 2980
[43] Bachelet G B, Hamann D R and Schlüter M A 1982 *Phys. Rev.* B **26** 4199
[44] Schroeder T *et al* 2007 *J. Appl. Phys.* **102** 034107
[45] Ernst F and Pirouz P 1988 *J. Appl. Phys.* **64** 4526
[46] Bollmann W 1967 *Phil. Mag.* **16** 363
[47] Zaumseil P and Schroeder T 2008 *J. Appl. Phys.* **104** 023532
[48] Liu S, Jayanthi C S, Wu S-Y, Qin X, Zhang Z and Lagally M G 2000 *Phys. Rev.* B **61** 4421
[49] Alfonso D R, Wu S-Y, Jayanthi C S and Kaxiras E 1999 *Phys. Rev.* B **59** 7745
[50] Liu J P, Zaumseil P, Bugiel E and Osten H-J 2001 *Appl. Phys. Lett.* **79** 671
[51] Shriver D F, Atkins P W and Langford C H 1992 *Inorganic Chemistry* (Weinheim: VCH)
[52] Yeh C Y, Lu Z W, Froyen S and Zunger A 1992 *Phys. Rev.* B **46** 10086
[53] Vurgaftman I, Meyer J R and Ram-Mohan L R 2001 *J. Appl. Phys.* **89** 5815
[54] Ahn C H, Triscone J-M and Mannhart J 2003 *Nature* **424** 1016
[55] Tokura Y 2003 *Phys. Today* **07** 55
[56] Watanabe Y 1995 *Appl. Phys. Lett.* **66** 1770
[57] Suzuki M and Ami T 1996 *Mater. Sci. Eng.* B **41** 166